8. J. G. Roederer, *Rev. Geophys. Space Phys.* **10**, 599 (1972).
9. A. Mogro-Campero and R. W. Fillius, *J. Geophys. Res.* **81**, 1289 (1976).
10. See J. H. Wolfe, J. D. Mihalov, H. R. Collard, D. D. McKibbin, L. A. Frank, and D. S. Intriligator [*Science* **207**, 403 (1980)] for plasma results during encounter.
11. K. Aksnes and F. A. Franklin, *Icarus* **36**, 107 (1978).
12. We thank R. Finnel, C. Hall, J. Wolfe, and especially R. Hogan for their attention and assistance in carrying out the successful Pioneer 11 mission. Discussions with T. G. Northrop concerning interpretation of the data are gratefully acknowledged. Our programming and data-processing team of N. Lal, H. Domchick, and J. Broomhall did an outstanding job of processing the encounter data in near real time. We also thank E. J. Smith and coinvestigators for supplying the magnetic field data from the helium vector magnetometer and M. Acuna and N. Ness for data from the high-field, flux-gate magnetometer.

3 December 1979

Trapped Radiation Belts of Saturn: First Look

Abstract. *Pioneer 11 has made the first exploration of the magnetosphere and trapped radiation belts of Saturn. Saturn's magnetosphere is intermediate in size between Earth's and Jupiter's, with trapped particle intensities comparable to Earth's. The outer region of Saturn's magnetosphere contains lower energy radiation and is variable with time; the inner region contains higher energy particles. The pitch angle distributions show a remarkable variety of field-aligned and locally mirroring configurations. The moons and especially the rings of Saturn are effective absorbers of trapped particles; underneath the rings, the trapped radiation is completely absorbed. We confirm the discovery of a new ring, called the F ring, a new division, the Pioneer division, and a moon, called 1979 S 2. The latter has probably been seen from Earth. There may be evidence for more bodies like 1979 S 2, but at this stage the interpretation of the data is ambiguous. Using particle diffusion rates, we estimate that the cross-sectional area of the F ring is* $> 7 \times 10^{13}$ *square centimeters and that the opacity is* $> 10^{-5}$. *Cosmic-ray albedo neutron decay should be looked into as a source of energetic particles in the inner magnetosphere of Saturn.*

On its historic flight past Saturn, Pioneer 11 carried instrumentation for the measurement of magnetospheric particles and fields. One of these instruments was a trapped radiation detector package designed and built at the University of California, San Diego (UCSD) (Table 1). Data obtained with this package are providing (i) confirmation of the existence of a magnetosphere and trapped radiation belt at Saturn, (ii) greater understanding of that magnetosphere and measurements of trapped particle fluxes and energies, (iii) the opportunity to investigate particle acceleration processes under new conditions and to compare them with activity in other magnetospheres, and (iv) information about ring and satellite absorption effects, including the wake of what is probably a previously undiscovered object.

Traveling to Saturn by way of Earth and Jupiter, Pioneer 11 crossed three magnetospheres and, with its sister spacecraft Pioneer 10, gathered excellent material for comparative studies. Figure 1 shows the intensities and radial extents of particles in a common energy range at the three planets. Other comparative features that can be seen include the effects of moons and rings and the modulation of the radiation levels by planetary rotation.

Earth's moon is well outside the terrestrial magnetosphere and has no effect on it. However, many of the moons of Jupiter and Saturn are inside the zone of trapped radiation and interact strongly with the trapped particles. In Fig. 1, the arrows at the orbits of Io and Amalthea point to dips caused by absorption of the radiation. There are analogous absorption features at Saturn, too, but they are not shown distinctly in Fig. 1. The ring of Jupiter (*1*) produces an absorption dip like that of the moons (*2*), but the rings of Saturn produce the most dramatic effect of all. The trapped radiation is completely absorbed at the outer edge of the A ring and, on lines of force intercepted by the Saturn rings, cosmic rays fall to less than one fifth of their interplanetary level. Our counting rates here were the lowest recorded in the entire flight.

Modulation at the planetary rotation rate is visible only at Jupiter, where the gross intensity variations outside the orbit of Io carry the 10-hour period of Jupiter's rotation. Earth's magnetosphere could produce a 24-hour modulation if an observatory could be held stationary at a chosen location. However, the near-Earth data shown here span only 1 hour, so there is no chance of seeing such an effect. Like Jupiter, Saturn has a rotation period of 10 hours, but if modulation occurs at this frequency, it is not readily apparent. It is natural to attribute this uniqueness to the remarkable symmetry of Saturn's magnetic field, which has a dipole moment with near-zero values for both tilt and offset (*3*).

Figure 2, A to C, shows a time profile (*4*) of Saturn's magnetosphere as seen by several channels of the UCSD instrument. Refer to Fig. 3 for the encounter geometry and Table 1 for a description of the detectors.

The outer region of Saturn's magnetosphere extends from ~ 6 Saturn radii (R_S) (*5–7*) to the magnetopause. It is strongly influenced by the time-variable solar wind, and it contains particles of lower energy than the inner region. Pio-

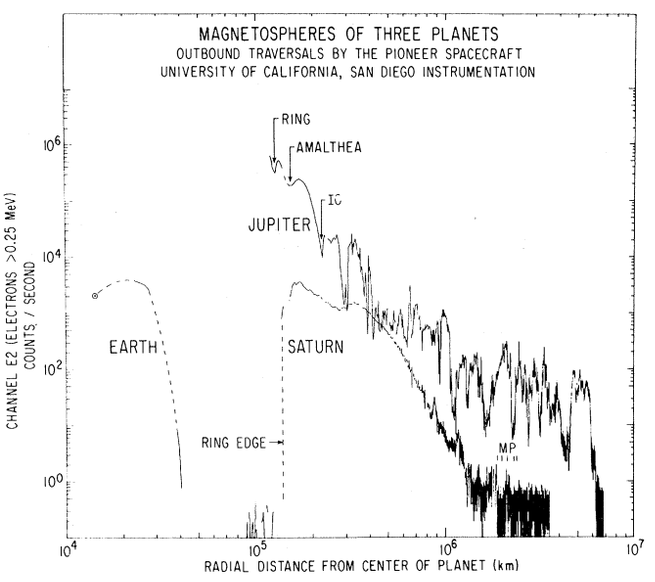

Fig. 1. Magnetospheres of three planets. These profiles of the radiation belts of Earth, Jupiter, and Saturn were made by University of California instrumentation on two Pioneer spacecraft. The profile of Earth's radiation belt was made in the dawn sector by Pioneer 10; those of Jupiter and Saturn were made by identical instrumentation on Pioneer 11 outbound in the noon and dawn sectors, respectively. The data shown are from an electron scatter detector with a geometric factor of 1.04 × 10^3 cm^2 sr^{-1} for electrons > 0.255 MeV. In the Jupiter magnetosphere inside Io, this detector responded mainly to omnidirectional electrons penetrating the shielding. For these particles the energy threshhold is 35 MeV and the geometric factor 0.038 cm^2. Note that the abscissa is in kilometers. To normalize to planetary radii, divide by 6371 km for Earth, 71,372 km for Jupiter, and 60,000 km for Saturn.

0036-8075/80/0125-0425$01.50/0

neer 11 entered this region inbound at 17.3 R_S (*8*) and, as seen at the extreme left of Fig. 2, A to C, the magnetopause crossing produced a jump of an order of magnitude in the counting rates of our low-energy channels. The outbound crossings are shown in Fig. 1: the intensity jumps outbound are much less prominent, since the trapped intensities were low and statistically irregular. Apparently, the reason for this difference lies not only in the local times of the inbound and outbound passes but also in a large temporal change in the magnetosphere during the Pioneer 11 flyby. As reported by Wolfe *et al.* (*8*), the spacecraft entered the magnetosphere at a time when it was compressed by a high-pressure solar wind stream. When it left, the solar wind pressure was lower, and presumably the magnetosphere was larger and the radiation less energetic.

The outer region contains several features that we tentatively attribute to temporal fluctuations. One such feature is the broad dip observed in low-energy electron intensities at about 0600 on day 244 (inbound near 10 R_S). Since this dip did not reoccur during the outbound pass, it does not seem to be a spatial phenomenon. It might be associated with the decompression of the magnetosphere and with growth of the diamagnetic ring current reported in this location by Smith *et al.* (*3*).

Another feature, observed at about 0900 on day 245 (~ 15 R_S outbound), occurred simultaneously with a large change in the magnetic field direction (*3*). The angular distributions of the low-energy particles underwent dramatic changes here also. It will take more analysis to describe the event fully; however, we are inclined to view this as a large temporal change, associated possibly with a magnetic tail and triggered by a change in interplanetary conditions.

The feature observed at about 1600 on day 245 (~ 20 R_S outbound) might be another temporal fluctuation, or it might be associated with Titan, since the spacecraft made its closest approach (~ 6 R_S) to Titan at this time and crossed its orbit shortly thereafter (*9*). The particle fluctuations were accompanied by a variation in the magnetic field (*3*). If this event is related to Titan, it implies that Titan itself is a source of energetic charged particles in Saturn's magnetosphere.

As Fig. 2C shows, during a large portion of the outbound pass the low-energy electron detector recorded a much higher flux when it faced parallel to the magnetic field than when it faced perpendicular. We think that this may be a manifestation of L-shell splitting (*10*) brought about by the change of the magnetic field geometry from highly compressed on the noon side to elongated at dawn. If this hypothesis is correct, quantitative modeling may tell us something about the field configuration in regions not sampled by the spacecraft.

Throughout the flyby, the pitch angle distributions underwent remarkable changes and, as shown by Trainor *et al.* (*11*), these changes varied with energy. Figure 4 shows the behavior of electrons in one energy range. If one ignores the noisy patches of data, one can see that the phase θ_2 tends to fall at either 0° or 90°, representing field-aligned (dumbbell) and perpendicular (pancake) angular distributions, respectively. These two patterns are familiar from both Earth and Jupiter, but are rarely seen to switch so

Table 1. Characteristics of the Pioneer 11 trapped radiation detector at Saturn encounter (September 1979). The detector has survived the Saturn radiation belt with no failures and no damage. However, because the radiation environment of Saturn is different from that of Jupiter or interplanetary space, some of our data channels count different types of particles than before. The main cause of these differences is the comparative absence of multi-MeV electrons at Saturn. The Cerenkov detector and channels M1 and M2 are most affected. Also, at Saturn there is little penetrating background on channels E and S. The ratios of their counting rates reveal that the three pulse height levels on detector M all responded to protons > 80 MeV (M1:M2:M3 = 3.3:1.4:1). By contrast, the signature of electrons at Jupiter was 1000:100:1. We could not measure the number of individual particles that were energetic enough to trigger the Cerenkov detector. However, inside 5 R_S the intensity of lower energy particles was sufficient to cause pileup; that is, several particles arriving closer together than the resolution time of the electronics add up to create a large pulse. The rate at which pileup events occur can be estimated by using the Poisson probability distribution function for an m-fold coincidence: $P_m = (\nu\tau)^m \exp(-\nu\tau)/m!$, where τ is the coincidence resolving time and ν is the primary rate of the single pulses (the rate when $\tau = 0$). The rate of n-fold coincidences ν_n is the product νP_{n-1} of the single rate and the probability that $n - 1$ pulses preceded any single pulse to create an n-fold coincidence. Then $\nu_n = \nu^n \tau^{n-1} \exp(-\nu\tau)/(n-1)!$. By comparing the rates on the three pulse height channels and the total current on the CDC channel, we can tell that channels C1 and C2 count mostly pulses whose height is 13 photoelectrons and whose rate can be determined from the equation above. Then, from the known properties of the detector and the dimensions of the instrument housing, we deduce that these pulses are caused by electrons of energy > 2 MeV and that the instrument geometric factor is ≃ 20 cm² sr for these particles. The data from detector C are taken from the CDC channel to assure linearity, with a calibration constant of 2.8×10^{14} count sec^{-1} A^{-1} derived from the pileup analysis given above.

Detector name and description	Channel	Discrimination level	Particle selectivity	Geometric factor
Cerenkov counter:	C1	> 31 photoelectrons	Pileup of 2-MeV electrons	20 cm² sr
Water-methanol radiator (index	C2	> 65 photoelectrons	Pileup of 2-MeV electrons	20 cm² sr
of refraction, 4/3) monitored by	C3	> 135 photoelectrons		
a photomultiplier tube with pulse and current output	CDC	$10^{-14} - 10^{-5}$ A	> 2-MeV electrons	7.3×10^{-14} A e^{-1} cm² sec sr
Electron scatter counter:	E1	> 0.089 MeV	> 0.16-MeV electrons	1.3×10^{-2} cm² sr
Silicon surface barrier diode	E2	> 0.19 MeV	> 0.255-MeV electrons	1.04×10^{-2} cm² sr
detector with a crooked aperture to admit scattered particles only	E3	> 0.40 MeV	> 0.460-MeV electrons	5.7×10^{-3} cm² sr
Minimum ionizing particle counter:	M1	> 0.40 MeV	> 80-MeV protons	0.038 cm²
Silicon surface barrier diode	M2	> 0.85 MeV	> 80-MeV protons	0.027 cm²
detector inside omnidirectional shielding (8 g cm^{-2})	M3	> 1.77 MeV	> 80-MeV protons	0.021 cm²
SP scintillator:	SPDC		> 100-keV protons	7.4×10^{-23} A eV^{-1} cm² sec sr (p)
Zn-S (Ag) phosphor (thickness,		$10^{-14} - 10^{-5}$ A	> 10-keV electrons	7.4×10^{-23} A eV^{-1} cm² sec sr (e)
1.5 mg cm^{-2}) monitored by a vacuum photodiode				
SE scintillator:	SEDC		> 100-keV protons	2.0×10^{-24} A eV^{-1} cm² sec sr (p$^+$)
Plastic scintillator (thickness,		$10^{-14} - 10^{-5}$ A	> 10-keV electrons	1.4×10^{-23} A eV^{-1} cm² sec sr (e$^-$)
1.5 mg cm^{-2}) monitored by a vacuum photodiode				

frequently or to have such large amplitudes. Information about this interesting behavior may ultimately be utilized in testing different physical mechanisms operating in Saturn's magnetosphere at the time of the encounter.

As the spacecraft approaches Saturn, the particle intensities increase, the spectrum hardens, and the higher energy channels are activated (this trend can be seen in Fig. 2). These are the characteristics of the usual pattern, in which particles are injected from the solar wind at the outer boundary and diffuse inward, breaking the third adiabatic invariant and conserving the first two (*12*).

However, at $\sim 6\ R_S$ there is an unexpected loss of low-energy particles (electrons and protons of $< \sim 0.5$ MeV). Because this feature occurs outbound as well as inbound, and because these particles appear to be permanently lost inside this distance, we believe that this is a spatial boundary rather than a temporal feature. We do not know the cause for the loss of these particles; possibilities include sweeping by the several known moons that orbit at and below this distance, absorption by a very tenuous material ring, and pitch angle scattering of the trapped radiation into the planetary loss cone by increased hydromagnetic wave activity. We note, however, that the electron pitch angle distribution turns from dumbbell-shaped to pancake-shaped where the losses begin (Fig. 4). Two of the suggested mechanisms, pitch angle scattering and absorption by a ring, would be expected to produce isotropy—not what is observed.

This low-energy particle cutoff is the boundary that we chose to separate the outer and inner regions of the magnetosphere. The inner region contains the higher energy particles that survive this hazard. These particles meet their fate at the outer edge of the visible ring system. As their bouncing motion causes the trapped particles to cross and recross the ring plane every few seconds, the optical depth of the ring material is multiplied by the number of particle bounces, and this product reaches unity before the trapped particles can diffuse past the obstacle. Only the two low-energy scintillators (the S detectors) recorded any substantial signal inside the outer edge of the A ring, but we believe that this signal was not caused directly by trapped radiation. The most likely explanation is that the thin cover foil was broken and the detectors responded to sunlight reflected by the rings and planet. Alternatively, they could have been sensing x- or ultraviolet radiation created by particle bombardment of the ring material.

A very strange feature, shown in Fig. 2, is a lack of symmetry in particle intensities between inbound and outbound passes. The intensities are significantly different and, equally remarkable, the

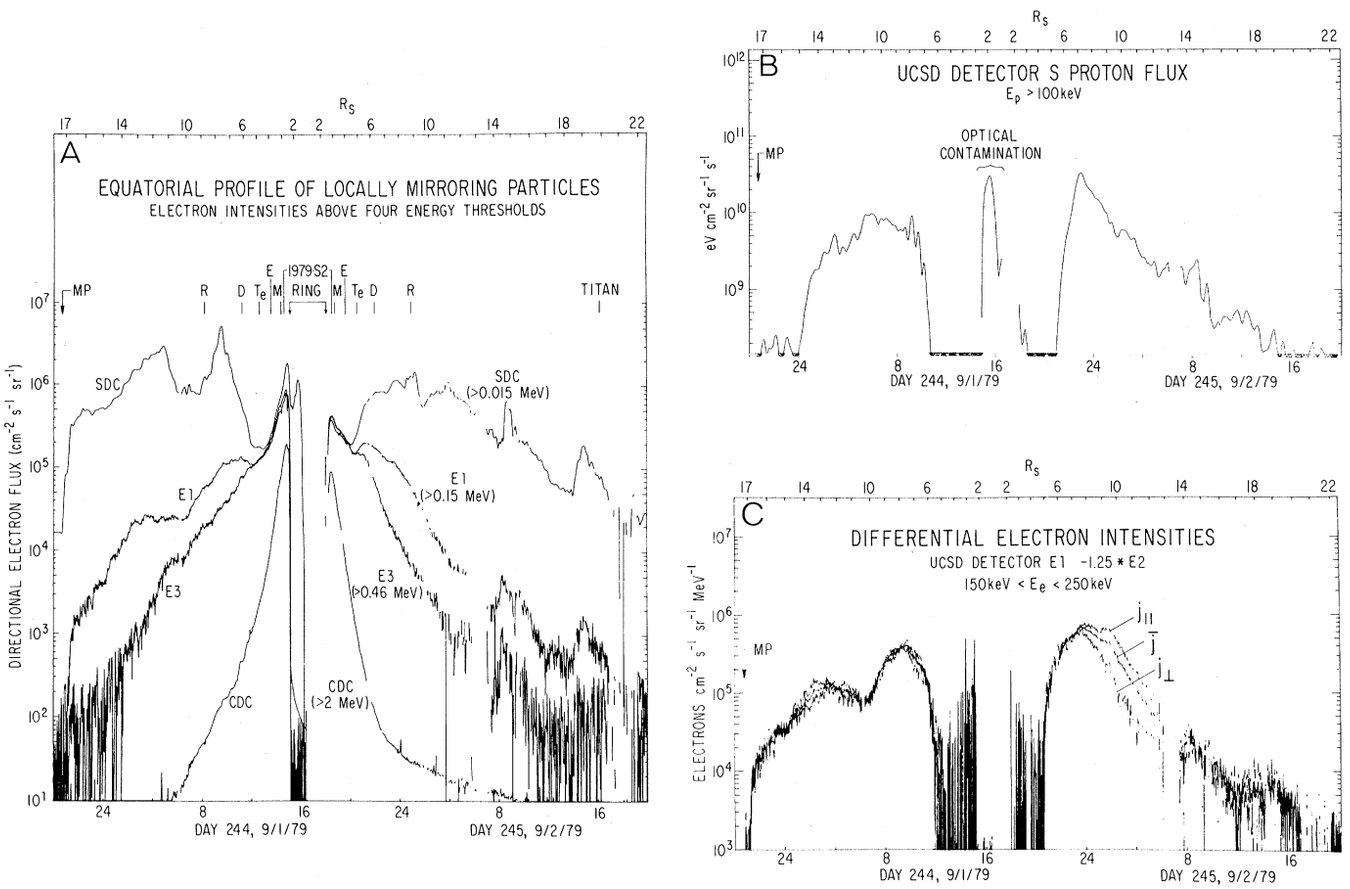

Fig. 2. Equatorial profiles of locally mirroring particles. The magnetopause crossing is marked *MP*. The orbits of Saturn's moons Rhea, Dione, Tethys, Enceladus, and Mimas are marked by *R*, *D*, T_e, *E*, and *M*, respectively. As the spacecraft spins and the viewing orientation of the trapped radiation detector is perpendicular to the spin axis, the detectors direct perpendicular to the magnetic field line twice during each spacecraft revolution. The intensity in this direction—that is, the directional flux of particles with 90° pitch angle, is shown here. (A) Electron intensities above four energy thresholds. The trace labeled *SDC* is a linear combinator of SPDC and SEDC outputs chosen to give the intensity of electrons only. As the detector is calibrated for energy flux (eV cm^{-2} sec^{-1} sr^{-1}), an average energy of 15 keV was used to convert to number flux (cm^{-2} sec^{-1} sr^{-1}). (B) Energy flux of protons above 100 keV. The trace is a linear combination of SPDC and SEDC outputs chosen to give the intensity of protons only. The detection threshold is approximately 2×10^8 eV cm^{-2} sec^{-1} sr^{-1}. (C) Electron intensity profiles at different pitch angles in the differential energy range $150 < E_e < 250$ keV. Also shown are the spin-averaged intensity and the intensity at the minimum pitch angle sampled. The differential energy band is a weighted difference between the outputs of two integral channels. For $L < 6\ R_S$ the difference is smaller than the statistical uncertainty in the integral channels, and the result is large amplitude random noise. These fluctuations are easily recognized and should be ignored.

asymmetry is different for different particles. For electrons from 0.5 to 2 MeV just outside the visible rings, the fluxes are higher inbound than outbound by a factor of about 2. For ~ 0.2-MeV electrons and ~ 150-keV protons at 6 R_S, the flux is higher outbound than inbound. However, for ~ 15-keV electrons at 6 R_S, the flux is higher inbound than outbound. Finally, although it is not shown in Fig. 2, the flux of 80-MeV protons just outside the rings is the same inbound and outbound. Since there are no magnetic field differences to account for these asymmetries (*3*), some combination of time variations in the radiation belts, large spatial electric fields, and electrostatic charge on the spacecraft (*13*) may explain these effects.

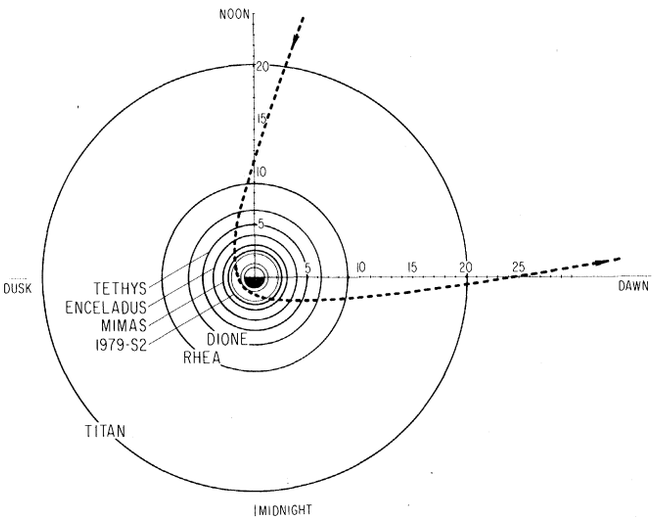

Fig. 3. Pioneer 11 encounter trajectory. The inclination of the trajectory was less than 6°, so this is essentially an equatorial profile.

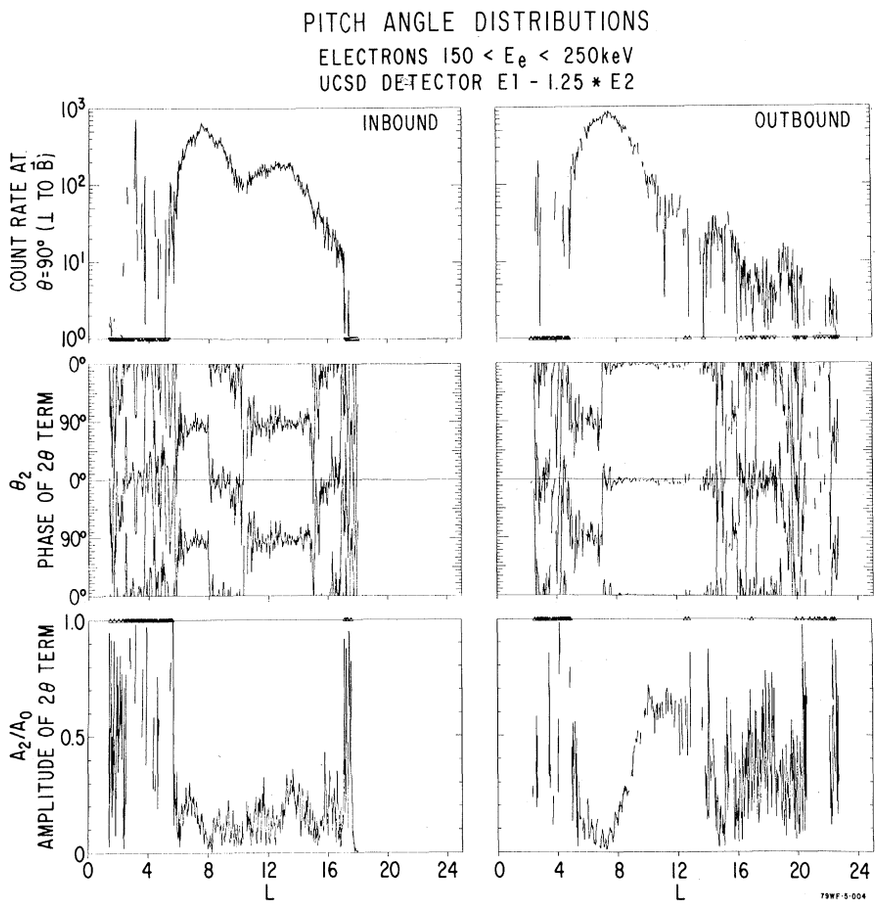

Fig. 4. Analysis of the angular distributions of electrons in the energy range $150 < E_e < 250$ keV. As in Fig. 2C, the weighted difference of two integral channels creates a differential energy passband centered at 200 keV. This technique reduces ambiguity when the angular distributions are energy-dependent. The data have been analyzed by a least-squares fit to the function $A(\theta) = A_0 + A_1 \cos(\theta - \theta_1) + A_2 \cos 2(\theta - \theta_2) + A_4 \cos 4(\theta - \theta_4)$, where θ is measured from the projection of the magnetic field vector onto the spin plane. The phase θ_2 ranges from −90° to 90° only, and the vertical scale wraps around at these limits to show the data twice and avoid cutting the pattern. We caution that A_2/A_0 and θ_2 tend to be random when A_0 is too small to be statistically significant. In some cases (for example, for $L < 5\ R_S$), A_0 fails this test because of statistical errors from the integral channels.

Figure 5 shows major features of Saturn's inner magnetosphere, constructed from data obtained during the Pioneer 11 inbound pass (a schematic of the trajectory is given in Fig. 6). The disappearance of trapped radiation at the outer edge of the rings has already been noted. However, the structure in this cutoff is a new and highly meaningful feature. The dip at 2.35 R_S confirms the discovery by the Pioneer 11 imaging photopolarimeter team (*4*) of a new ring, dubbed the F ring. The relative maximum to the left of this dip shows the profile of the interval between the A and F rings that was named the Pioneer division by Gehrels *et al.* (*14*). Broad absorption dips appear in the proton profile at the orbit of Mimas and at another position that is marked 1979 S 2. This latter evidently marks the orbit of one or more objects that may have been sighted previously, but whose orbital elements were too uncertain or inaccurate to permit positive identification (*15*).

There is a clear distinction between the profiles of the electron intensity ($E_e > 0.05$ MeV) and of the proton intensity ($E_p > 80$ MeV). The electrons seem to be enjoying the same advantage, against being swept up by these objects, that we observed previously at the orbit of Io in the Jupiter radiation belts (*16*). A combination of the corotational electric field and the curvature and gradient of the magnetic field gives them a drift velocity that is nearly synchronous with the Keplerian periods of the orbiting bodies. Thus they have a low probability of encountering the objects while radial diffusion carries them past their orbits. As the protons are carried in the opposite direction by the magnetic field curvature and gradient drifts, the probability of their having an encounter is enhanced. The sweeping of the protons appears to be complete at Mimas and 1979 S 2, whereas the reduction of the electron intensity appears negligible.

The spike marked 1979 S 2, one of the most remarkable events of the flyby, is shown in high time resolution in Fig. 7. For an interval of just 9 seconds, the counting rates of our detectors fell to ~ 1 percent of the neighboring values [simi-

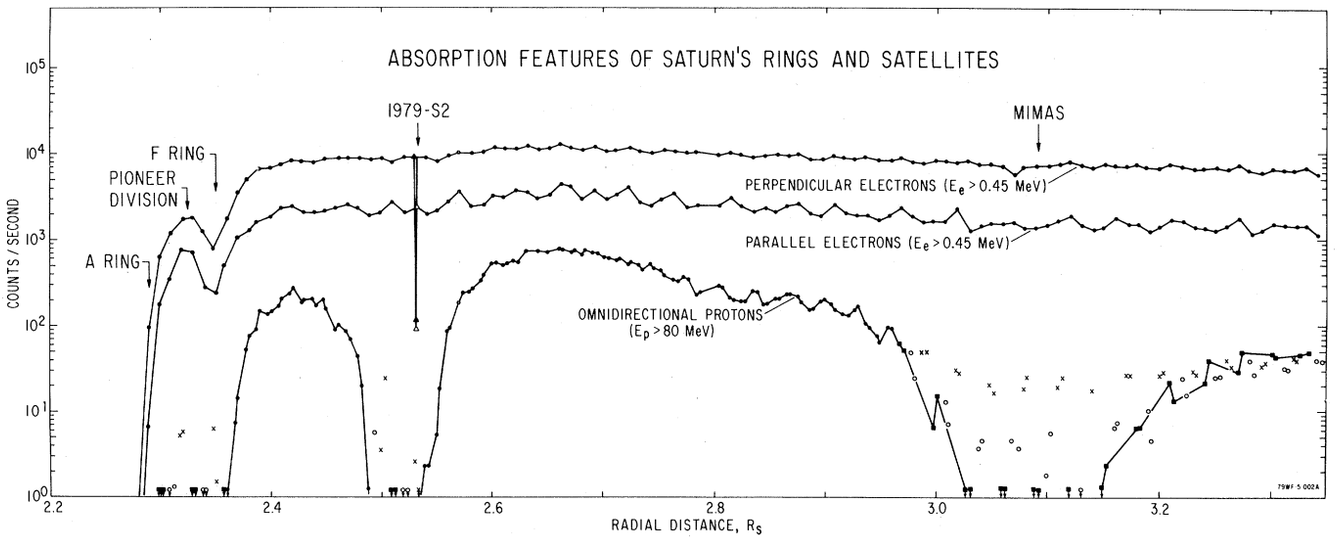

Fig. 5. Absorption features of Saturn's rings and satellites. This graph exhibits data from detectors E and M; all three channels of each are used to gain time resolution. To normalize them to channel E1, we multiplied the channel 3 counting rates by 2.8 and the E2 rates by 1.25, their relative efficiencies for electrons > 0.5 MeV. Detector E is directional, and the maximum and minimum readings from each electron sample have been plotted and labeled perpendicular and parallel, respectively. The bottom trace was made from normalized M detector data. Since the detector response is nearly isotropic, every reading is shown regardless of orientation. This detector responds to electrons > 10 MeV and protons > 80 MeV, the particles being identified by the three channels of pulse height information. The electron component contributes from 30 to 70 count sec^{-1} to channel M1. To show the proton profile below $L = 3$, electrons have been deducted from channel M1 by subtracting 0.0072 times the perpendicular E detector rate and from channel M2 by subtracting 0.0015 times the same rate (M3 needs no subtraction). After this correction, channels M2 and M3 were normalized to M1 by multiplying by 1.4 and 3.3, respectively, their relative efficiencies for protons. For $L > 3$, no subtraction was performed before scaling the channels. At the position of Mimas, a drop-off in the proton profile is shown by channel M3 (■—■). The flat electron profile is visible in channel M1 (x), and the pulse height signature of electrons can be seen during the proton drop-off. In the dip at 1979 S 2, electrons are subtracted and all the normalized data are connected by a line to emphasize the proton drop-off.

lar effects were registered by the other charged particle instruments as well (*17*)]. Outside the sharp minimum, the electron flux shows no sign of depletion and the proton flux is in the middle of a broad depression. The only explanation for such a sharp effect is that Pioneer 11 crossed through, or very close to, the flux tube connected to a large orbiting object. The object is being called 1979 S 2, even though it is probably identical to the object sighted shortly before by the Pioneer 11 imaging instrument (*14, 15*). Since the planetocentric radial velocity of the spacecraft is 16.4 km/sec at this position, the diameter of 1979 S 2 can be taken to be at least 150 km. It could be larger if the electron drop-off is the cross section of a wake that had begun to fill in, or if Pioneer 11 went through the flux tube connecting to 1979 S 2 but missed the major diameter.

The orbit of 1979 S 2 may be eccentric, since the electron drop-off is noticeably not in the center of the proton absorption zone. Using $2ae$ for the sweeping width of an eccentric orbit, where a is the semimajor axis and e is the eccentricity, one can deduce that $a = 2.52 \pm 0.01\ R_S$ and $e = 0.010 \pm 0.002\ R_S$. These values could change if the magnetic field is shown to have a significant offset. However, this reasoning is confirmed at the Mimas orbit, where the width of the proton sweeping zone, $0.12 \pm 0.02\ R_S$, yields $e = 0.02 \pm 0.003\ R_S$, which agrees with tabulated values (*18*). On the other hand, if we restrict the orbit of the new satellite to perfect circularity, then more than one satellite may contribute to the sweeping of the 80-MeV protons in this region (*17*).

One can also make quantitative inferences about the F ring from trapped radiation measurements. In Fig. 5, the position and width can be read as $2.35 \pm 0.005\ R_S$ and $\lesssim 0.02\ R_S$, respectively. Bounds can be placed on the total cross-sectional area, mass, and opacity by comparing the sweeping rate of the ring with that of 1979 S 2 and Mimas. We use a statistical sweeping model in which loss rate $-dn/dt$ is proportional to particle density n times some probability p of absorption per unit of time t:

$$\frac{dn}{dt} = -np \qquad (1)$$

We picture the ring as an annulus of width W containing a randomly spaced collection of small objects whose cumulative cross-sectional area is given by A. Every time a trapped particle crosses the equator, its chance of hitting one of the objects is $A/(2\pi\ 2.35\ R_S\ W)$. Thus

$$p = \frac{2}{T_b}\,\frac{A}{2\pi\ 2.35\ R_S\ W} \qquad (2)$$

where T_b is the particle's bounce period. Equation 1 expresses the loss rate during the time it takes the particle to diffuse across the ring; that is, from $t = 0$ to $t = W/V$, where V is the particle's radial diffusion velocity. Integrating Eq. 1 between these limits and using Eq. 2, we obtain

$$A = -\ln\left(\frac{n}{n_0}\right)\frac{T_b}{2}\,2\pi\ 2.35\ R_S\ V \qquad (3)$$

where n/n_0 is the fraction of particles that diffuse safely past the hazard.

All the parameters on the right-hand side of Eq. 3 are known except V, which we obtain by analysis of absorption at the moons. However, for moons the longitudinal distribution of absorbing material is not random; the particle and moon meet only when their relative azimuthal motion brings them past the same longitude. Hence

$$p = \frac{d_{\text{eff}}}{P\ L} \qquad (4)$$

(*2, 19*) where d_{eff} is the sum of the moon's diameter d plus twice the particle's gyroradius r_g, P is the moon's period in the drift frame of the particles, and L is an arbitrary radial diffusion length $>> d_{\text{eff}}$.

Using Eq. 4 and integrating Eq. 1 as before from $t = 0$ to $t = L/V$, we obtain

$$V = \frac{-d_{\text{eff}}}{P \ln (n/n_0)} \qquad (5)$$

Table 2. Diffusion velocities past Mimas and 1979 S 2.

Parameter	Electrons (~ 1 MeV)		Protons (~ 80 MeV)	
	Mimas	1979 S 2	Mimas	1979 S 2
r_g (km)	6.4	3.5	1770	940
d (km)	400 ± 100	> 150	400 ± 100	> 150
d_{eff} (km)	410	> 160	3950	≳ 2040
P (hours)	100	300	0.2	0.25
n/n_0	> 19/20	> 19/20	< 1/400	< 1/1500
V (cm sec^{-1})	> 2.2 × 10^3	> 280	< 9.2 × 10^4	≲ 3.1 × 10^4
V (R_s year^{-1})	> 11	> 1.4	< 460	≲ 160

Note that L cancels out of the result. Because there appears to be complete transmission of electrons and complete absorption of protons, we can only give limits for the fraction of particles that survive, and we can only deduce limits on the radial diffusion velocities. Table 2 shows some of the parameters and results of Eq. 5 for 1-Mev electrons and 80-MeV protons at Mimas and 1979 S 2.

At the F ring there appears to be complete absorption of protons and ~ 90 percent absorption of electrons. Because the protons are diffusing immeasurably slowly, an infinitesimal amount of material might be enough to stop them; but the lower limit on the electron diffusion velocity tells us that at least enough material is present to absorb electrons that are diffusing into the ring at this rate. Thus Eq. 3 gives a lower limit for the cross-sectional area of the F ring. By using $n/n_0 = 10$ percent, $T_b = 2.5$ seconds, and the limit on V at 1979 S 2, we get, for the cross-sectional area of the F ring, $A > 7 \times 10^{13}$ cm^2. If the ring particles are uniform with radius h centimeters and density ρ grams per cubic centimeter, the total mass of the ring is at least $> 1 \times 10^{14}\ \rho\ h$ grams. The opacity depends on the radial width over which the ring material is distributed. Since the ring occupies the space $2\pi\ 2.35\ R_S\ W = 9 \times 10^{10}\ W$ cm^2, the opacity τ is bounded by $\tau > 10^3/W$, where W is in centimeters. By using the upper limit to W obtained from Fig. 5, we find a lower bound of $> 10^{-5}$ for τ.

In summary, then, our charged particle data give the following physical parameters for the new satellite 1979 S 2 and the F ring: for object 1979 S 2, the semimajor axis = 2.52 ± 0.01 R_S, eccentricity = 0.010 ± 0.002, and diameter ≥ 150 km; for the F ring, the semimajor axis = 2.35 R_S, width < 10^8 cm, area > 7 × 10^{13} cm^2, mass > 1 × $10^{14}\ \rho\ h$ grams, and opacity > $10^3/W$.

There may be evidence for still more moons (*17, 20*). For instance, close inspection of the traces in Fig. 5 reveals a slight concavity in the proton contour at ~ 2.8 R_S—the position given for an earlier, unconfirmed, sighting of a moon tentatively called Janus. This feature is more prominent on the outbound pass, and could be due to sweeping by an orbiting object. However, the object must be tiny to produce such a small effect compared to those of Mimas and 1979 S 2, and it seems questionable that such an object would have been visible from Earth.

The apparent total absorption of 80-MeV protons by Mimas and 1979 S 2 presents an interesting paradox. If the protons of the inner magnetosphere come from the inward diffusion of solar wind particles, how do any get inside these totally absorbing barriers? Two possible explanations are: (i) the inner region is filled during times of higher particle mobility—such as magnetic storms—and (ii) the protons are created in place. The possibility that the particles come from the decay of albedo neutrons created by collisions of cosmic rays with the upper atmosphere and rings of Saturn should be investigated. Called CRAND for cosmic-ray albedo neutron decay, this mechanism is one of the first that was proposed to explain the high-energy component of Earth's radiation belt (*21*).

For CRAND to be an adequate source of protons, the injection rate must be equal to the loss rate. The loss rate is $(J_p/v)/T_p$, where T_p is the proton trapping lifetime, J_p is the trapped proton flux, and v is the proton's velocity. If absorption by the moons is the dominant loss mechanism, then $T_p = T_d$, the average time it takes to migrate to one of the sweeping channels. Treating the proton's radial motion as a random walk,

$$T_d = \frac{\langle \Delta L^2 \rangle}{2D} \qquad (6)$$

where $\langle \Delta L^2 \rangle$ is the mean squared displacement and D is the diffusion coefficient (*22*). The value for $\langle \Delta L^2 \rangle$ can be taken from the width of the region between Mimas and 1979 S 2, and we can use Fick's law (*23*) to obtain the diffusion coefficient

$$D = \frac{-V}{d(\ln n)/dL} \qquad (7)$$

By using 0.04 and 0.02 R_S for $[d(\ln n)/dL]^{-1}$ at Mimas and 1979 S 2, and taking V from Table 2, we get $D < 6 \times 10^{-7}$ and $D < 1 \times 10^{-7}\ R_S^2$ sec^{-1}, respectively. Then, for protons between Mimas and 1979 S 2, $T_d > 1$ day to 1 week.

The injection rate is $(J_n/v)/T_n$, where T_n is the neutron decay lifetime, J_n is the albedo neutron flux, and the neutron's velocity is the same as the proton's. Setting the injection rate equal to the loss

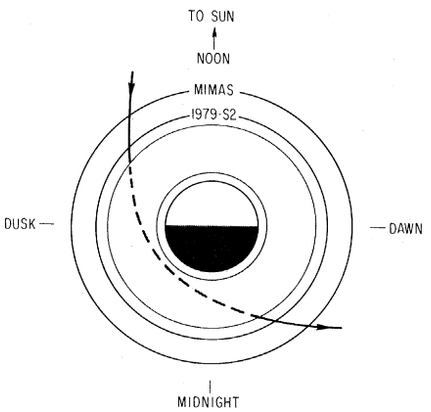

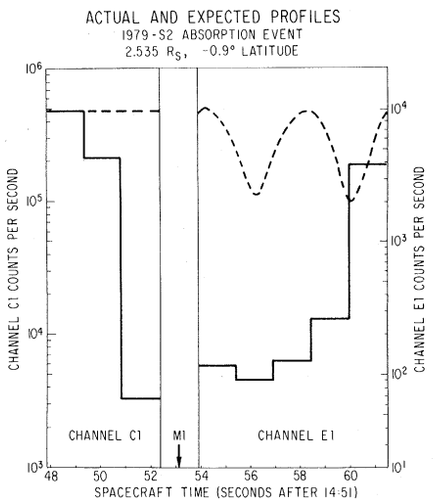

Fig. 6 (left). Trajectory of Pioneer 11 through the inner magnetosphere of saturn. Fig. 7 (right). Actual and expected profiles of the 1979 S 2 absorption event. Each reading from the UCSD instrument is shown for this interval, during which the internal commutator cycled through three channels—C1, M1, and E1. Each reading is a 1.5-second accumulation and is represented by the stepped bar graph. The M1 value was zero. The dashed line shows the counting rates expected on the basis of the neighboring readings. The expected profile of channel E1 reflects the spin modulation of the directional detector in a pancake angular distribution.

rate gives an expression for the proton-trapping lifetime that balances the CRAND source:

$$T_p = \frac{J_p}{J_n} T_n \quad (8)$$

At 2.7 R_S, the proton flux above 80 MeV is $\sim 2 \times 10^4$ cm^{-2} sec^{-1} and the neutron lifetime is 13 minutes. It is possible to calculate the neutron albedo flux at Saturn, but such an effort is beyond the scope of this report. To test the reasonability of our speculation, we merely write J_n as some factor F times the albedo neutron flux at Earth. The latter is ~ 0.1 cm^{-2} sec^{-1} for neutrons above 80 MeV (*24*), so we obtain, for the proton trapping lifetime that balances the CRAND source, $T = \sim 7.5/F$ years. If F is of the order of unity, this number is easily compatible with the diffusive loss time T_d. However, a more satisfying comparison must await a more extensive calculation.

W. FILLIUS
University of California, San Diego, La Jolla 92093

W. H. IP
Max-Planck-Institut für Aeronomie, Katlenburg-Lindau, West Germany

C. E. MCILWAIN
University of California, San Diego

References and Notes

1. B. A. Smith *et al.*, *Science* **204**, 951 (1979).
2. M. H. Acuña and N. F. Ness, *J. Geophys. Res.* **81**, 2917 (1976); W. Fillius, in *Jupiter*, T. Gehrels, Ed. (Univ. of Arizona Press, Tucson, 1976), pp. 896–927.
3. E. J. Smith, L. Davis, Jr., D. E. Jones, P. J. Coleman, Jr., D. S. Colburn, P. Dyal, C. P. Sonett, *Science* **207**, 407 (1980); M. H. Acuña and N. F. Ness, *ibid.*, p. 444.
4. All times given in this report are universal time at the spacecraft, which is obtained from ground-received universal time by deducting the one-way travel time of light (about 1 hour 26 minutes 20 seconds).
5. C. E. McIlwain, *J. Geophys. Res.* **66**, 3681 (1961).
6. In this report, L is the distance from the center of the planet to the equatorial crossing of the magnetic line of force through an observation point. It was computed by using a dipole field model with zero tilt and offset.
7. The unit of distance is the planetary radius, R_S, equal to 60,000 km.
8. J. H. Wolfe, J. D. Mihalov, H. R. Collard, D. D. McKibbin, L. A. Frank, D. S. Intriligator, *Science* **207**, 403 (1980).
9. J. W. Dyer, *ibid.*, p. 400.
10. E. C. Stone, *J. Geophys. Res.* **68**, 4157 (1963); J. G. Roederer, *Dynamics of Geomagnetically Trapped Radiaton* (Springer-Verlag, New York, 1970).
11. J. H. Trainor, F. B. McDonald, A. W. Schardt *Science* **207**, 421 (1980).
12. M. Schulz and L. J. Lanzerotti, *Particle Diffusion in the Radiation Belts* (Springer-Verlag, New York, 1974).
13. S. E. DeForest, *J. Geophys. Res.* **77**, 651 (1972).
14. T. Gehrels *et al.*, *Science* **207**, 434 (1980).
15. W. H. Blume *et al.*, in preparation.
16. R. W. Fillius and C. E. McIlwain, *J. Geophys. Res.* **79**, 3589 (1974); J. A. Simpson, D. C. Hamilton, R. B. McKibbin, A. Mogro-Campero, K. R. Pyle, A. J. Tuzzolino, *ibid.*, p. 3522.
17. J. A. Van Allen, M. F. Thomsen, B. A. Randall, R. L. Rairden, C. L. Grosskreutz, *Science* **207**, 415 (1980); J. A. Simpson *et al.* (*20*).
18. D. Morrison and D. P. Cruikshank, *Space Sci. Rev.* **15**, 641 (1974).
19. A. Mogro-Campero and W. Fillius, *J. Geophys. Res.* **81**, 1289 (1976).
20. J. A. Simpson, T. S. Bastian, D. L. Chenette, G. A. Lentz, R. B. McKibbin, K. R. Pyle, A. J. Tuzzolino, *Science* **207**, 411 (1980).
21. N. C. Christofilos, *J. Geophys. Res.* **64**, 869 (1959); P. B. Kellogg, *Nuovo Cimento* **11**, 48 (1959); S. F. Singer, *Phys. Rev. Lett.* **1**, 181 (1958); S. N. Vernov, special lecture to the Fifth General Assembly of the Comité Special de l'Année Geophysique Internationale, Moscow, 30 July to 9 August 1958.
22. F. Reif, *Fundamentals of Statistical and Thermal Physics* (McGraw-Hill, New York, 1974), pp. 486–488.
23. C. Kittell, *Elementary Statistical Physics* (Wiley, New York, 1958), p. 155.
24. R. E. Lingenfelter, in *Spallation Nuclear Reactions and Their Applications*, B. S. P. Shen and M. Merker, Eds. (Reidel, Dordrecht, Netherlands, 1976), pp. 193–205.
25. We are grateful to S. E. DeForest, E. Whipple, B. Johnson, J. Quinn, M. Greenspan, and C. Olson for assistance with the real-time data. C. Barnes, I. Goldman, and J. B. Blake made generous contributions to the detector calibrations, and E. Smith provided magnetometer data. Discussions with R. E. Lingenfelter were very helpful. The success of the Pioneer spacecraft reflects the superlative job done by the Pioneer Project Office under the leadership of C. F. Hall. This work was supported by NASA contract NAS 2-6552 and by NASA grant NGL-05-005-007.

3 December 1979

Ultraviolet Photometer Observations of the Saturnian System

Abstract. *Several interesting cloud and atmospheric features of the Saturn system have been observed by the long-wavelength channel of the two-channel ultraviolet photometer aboard the Pioneer Saturn spacecraft. Reported are observations of the most obvious features, including a Titan-associated cloud, a ring cloud, and the variation of atmospheric emission across Saturn's disk. The long-wavelength data for Titan suggest that a cloud of atomic hydrogen extends at least 5 Saturn radii along its orbit and about 1.5 Saturn radii vertically. A ring cloud, thought to be atomic hydrogen, has also been observed by the long-wavelength channel of the photometer; it shows significant enhancement in the vicinity of the B ring. Finally, spatially resolved observations of Saturn's disk show significant latitudinal variation. Possible explanations of the variation include aurora or limb brightening.*

The ultraviolet photometer on Pioneer Saturn covers two broad spectral regions (*1*, *2*). The short-wavelength (λ_S) band is sensitive only to emissions shortward of about 800 Å and includes the 584-Å resonance line of helium. The region of sensitivity of the long-wavelength (λ_L) channel includes the hydrogen resonance line at 1216 Å. The instrument design was based on the assumed dominance of hydrogen and helium gases in the Jupiter and Saturn systems. Accordingly, the emission signal in the λ_L channel is interpreted as resulting mainly from hydrogen emission at 1216 Å, while the signal in the λ_S channel is considered to be due to helium emission at 584 Å and perhaps other species that emit shortward of $\sim$ 800 Å.

The field of view of the photometer is limited by a mechanical collimator whose optical axis is oriented at an angle $\theta_0 = 20°$ with respect to the spacecraft spin axis. The scanning motion that results from spacecraft rotation sweeps the field of view over the surface of a 40° cone whose vertex is on the spacecraft spin axis and whose axis of symmetry is oriented along the spin axis. The spin axis of the spacecraft is parallel to the spacecraft-Earth line. Figure 1 shows the trajectory of the spacecraft and the field of view of the photometer projected on the Saturn equatorial plane near the Sat-

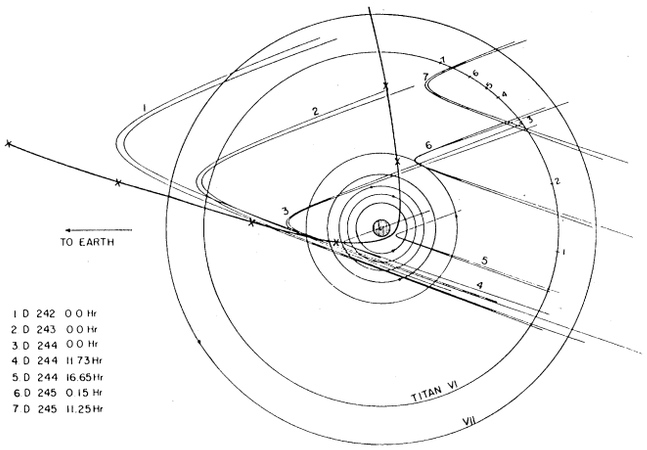

Fig. 1. Viewing hyperbolas in Saturn's equatorial plane as seen from above Saturn's north pole. The width of the hyperbolas represents the 1° cone angle width over which the photometer is sensitive. The view in the plane of the satellite orbits corresponds to seven different spacecraft positions indicated by the seven hyperbolas. Titan is at position 1 when the photometer view is that indicated by hyperbola 1.

0036-8075/80/0125-0431$00.75/0